Chemical Engineering Journal 382 (2020) 123038

Contents lists available at ScienceDirect

Chemical Engineering Journal

journal homepage: www.elsevier.com/locate/cej

Formation of surface ionization waves in a plasma enhanced packed bed reactor for catalysis applications

Zaka-ul-Islam Mujahid[a,*], Juliusz Kruszelnicki[b], Ahmed Hala[c], Mark J. Kushner[d]

[a] Department of Physics, Faculty of Science, Jazan University, Jazan 45142, Saudi Arabia
[b] University of Michigan, Dept. of Nuclear Engineering and Radiological Sciences, 2355 Bonisteel Boulevard, Ann Arbor, MI 48109-2104 USA
[c] King Abdulaziz City for Science and Technology (KACST), Riyadh, Saudi Arabia
[d] University of Michigan Dept. of Electrical Engineering and Computer Science, 1301 Beal Avenue, Ann Arbor, MI 48109-2122, USA

HIGHLIGHTS

- Plasma-Enhanced Packed Bed Reactor was studied experimentally and via 2-D modeling.
- Impacts of voltage amplitude and polarity were studied.
- 2D model was qualitatively validated through multiple-axis experimental diagnostics.
- At least three discharge types were found to exist at various applied voltages.
- Each discharge type led to different plasma properties, which impact selectivity.

ARTICLE INFO

Keywords:
Plasma catalysis
PROES
Microdischarge
Environmental applications

ABSTRACT

Plasma enhanced packed bed reactors (PE-PBRs) intrinsically have complex geometries which makes it difficult to apply conventional scaling laws. For example, controlling the manner of discharge propagation between the micro-discharges (MDs) that occur between dielectrics in PE-PBRs and surface ionization waves (SIWs) that propagate along the dielectrics would aid in selectivity during plasma catalysis. An important parameter in that optimization is the pulse power format. In this work, we investigated the role of applied voltage amplitude and polarity on time resolved dynamics in an atmospheric pressure dielectric barrier discharge (DBD) operating in helium having surface topology resembling PE-PBRs using phase and space resolved optical emission spectroscopy (PROES). To enable systematic studies, the DBD uses an array of dielectric semi-spheres imaged through a top transparent electrode and imaged between the two electrodes from the side. The results were compared with 2-dimensional modeling. We identified three discharge mechanisms: filamentary micro-discharges (F-MDs) in the volume (the space between the surface of the dielectrics and the counter electrode), surface micro-discharges (S-MDs) between the dielectric semi-spheres near their contact points, and SIWs over the curved or flat dielectric surfaces. At the lowest voltages, only F-MDs are generated, once in each half cycle. At intermediate voltages, SIWs also appear which transform into S-MDs at the contact points. When voltage is further increased, several additional pulses are observed, which generate S-MDs at the contact points or a combination F-MDs and S-MDs. The voltage amplitude determines the frequency of these pulses. Modeling results show variations in plasma density and electron temperature for each of the three mechanisms which, in turn, impact production of reactive species.

1. Introduction

Plasma enhanced packed bed reactors (PE-PBRs) are being investigated for several applications including gaseous pollution control and hydrocarbon gas conversion [1–6]. In its basic form, a PE-PBR is an atmospheric pressure plasma in which the discharge propagates through and over an array of dielectric pellets. Conventional thermally driven PBRs are used for chemical conversion aided by the catalytic properties of the dielectric which are often impregnated with metal catalytic particles [7]. The augmentation of conventional PBRs with plasma often enhances conversion efficiency and provides better product selectivity [7,8]. This synergistic effect may arise from the

* Corresponding author.
E-mail addresses: zmujahid@jazanu.edu.sa (Z.-u.-I. Mujahid), jkrusze@umich.edu (J. Kruszelnicki), mjkush@umich.edu (M.J. Kushner).

https://doi.org/10.1016/j.cej.2019.123038
Received 10 July 2019; Received in revised form 30 September 2019; Accepted 1 October 2019
Available online 03 October 2019
1385-8947/ © 2019 Published by Elsevier B.V.

enhanced chemical reactions of the catalyst due to its activation by the plasma, plasma produced reactant intermediates (e.g., radicals) at lower operating temperatures and changes in the plasma due to the presence of the catalytic (dielectric) pellets.

Several studies have addressed the properties of PE-PBRs using modeling [9–11]. For example, Van Laer and Bogaerts [9,10] used a two-dimensional (2D) fluid model of a PE-PBR sustained in helium. They found an enhancement of the electric field and electron temperature near the contact points between dielectric pellets which becomes more pronounced with pellets having higher dielectric constant. They also observed that the discharge mode changes with the applied potential from Townsend to glow modes.

Experimentally, researchers have investigated the propagation of plasmas through PE-PBRs using intensified charge-coupled-device (ICCD) camera imaging, which provides insights into the plasma ignition and sustainment mechanisms; and their dependence on location (e.g., discharges between pellets or along the surface of pellets). These investigations have been performed using randomly packed discharge beds [12–17], a single pellet [14,15,18,19] and an organized packing of the dielectric structures [11,20]. Using an organized structure [20], distinct modes of discharge propagation were observed. The discharge was sustained by surface micro-discharges (S-MDs) at the contact points of adjacent pellets, filamentary micro-discharges (F-MDs) in the volume between pellets and surface ionization waves (SIWs) over the surface of pellets. However, even in the ordered pellet lattices, it is difficult to quantify the axial location of the discharge at different phases of the applied voltage and discern the differences resulting from positive and negative polarities.

The pulse power waveform is one of the most important system parameters in optimizing a PE-PBR, including applied voltage amplitude, pulse shape and frequency, all of which contribute to the specific input energy (SIE) [21,22]. In varying the pulse power format, two discharge propagation mechanisms were identified – S-MDs at the contact points (referred to as point-to-point [13,14,16] or partial discharges [15,18]) and SIWs (also called “surface streamers” [15,18]). Wang et al. [17] found that the location of the discharge changes from the dielectric pellet surface to the contact points when increasing the dielectric constant of the pellets and applied voltage. Ogata et al. [13,14,16] found that discharge properties are not only influenced by the pulse power format but also by the surface properties of the catalyst, such as by the loading of metal nanoparticles or changing the Si/Al ratio of the pellet. They showed that loading metal nanoparticles on the surface of the dielectric beads spreads the plasma over a larger surface area compared to bare zeolites [14]. They also found that silver nanoparticle-loaded zeolites achieved the highest surface area coverage of the plasma and highest rate of decomposition of volatile organic compounds (VOCs).

The random arrangement of pellets in many of these investigations makes it difficult to translate scaling laws to other systems. Although time-averaged ICCD images provide keen insights to discharge behavior, additional information can be gained using time resolved imaging. For example, time averaged ICCD image of a dielectric barrier discharge (DBD) resembling a PE-PBR [20] suggested that the discharge is generated only at the contact points. For the same system, time and space resolved imaging showed three different plasma sustaining mechanisms occurring at different locations and times.

In this work, we expand on previous investigations [22], and report on the influence of applied voltage amplitude and polarity on three plasma sustainment mechanisms in a DBD using phase and space-resolved spectroscopy (PROES) and computational modeling. The surface of the DBD has an array of dielectric semi-spheres with the intent of making measurements in an ordered, optically accessible system that shares geometrical properties with PE-PBRs. The results show that the discharge sustainment mechanisms and method of propagation are sensitive functions of the voltage waveforms. Three discharge propagation mechanisms were observed: filamentary micro-discharges (F-MDs) in the gap between the dielectric semi-spheres and the top dielectric, surface micro-discharges (S-MDs) at the contact points of the semi-spheres, and surface ionization waves (SIWs) over dielectric surfaces. At the lowest applied voltage, only F-MDs occurred. With increasing voltage, SIWs appeared in addition to the first mechanism. With further increase in applied voltage, S-MDs also appear. The sequence and intensity of each discharge mechanism are sensitive to the polarity of the voltage.

The experimental setup and diagnostics used in this study are described in Section II, followed by a description of the model in Section III. Experimental results are described in Section IV and those from the model are discussed in Section V. Concluding remarks are in Section VI.

2. Description of the experiment

The objective of this work was to understand the role of applied voltage amplitude and polarity on plasma propagation and plasma-surface interactions in PE-PBR relevant systems. The conventional PBR arrangement (i.e., a cylinder randomly filled with spherical dielectric beads) does not enable sufficient optical access for quantitative experimental investigation. Therefore, a more accessible quasi-2D geometry has been developed, the patterned DBD (p-DBD), as shown in Fig. 1. The p-DBD mimics the spherical boundaries between the pellets in a PE-PBR, and while not a commercially configuration, it allows for expanded experimental investigation. The reactor is a parallel-plate-like DBD where one surface consists of a layer of dielectric semi-spheres that are organized to include both contact points and the empty volumes between them. This design enables optical access and is scalable in multiple dimensions. Further details on the p-DBD system are discussed in Ref. [20].

Briefly, the p-DBD is contained in 100 mm diameter, 10 mm high quartz ring (dielectric constant ε_r = 3.75–3.8) with two tubes for the gas inlet and outlet. The quartz ring is covered on the top and bottom with two 1 mm thick glass plates. The bottom borosilicate glass plate includes twelve semi-spherical dome structures having ε_r = 4.6, as shown in Fig. 1a, set on a grounded electrode. The dome structures are also made of borosilicate glass and have radii of curvature of 15 mm, spacing of 24 mm and height of 6 mm. The top glass plate is made of soda lime glass (ε_r = 7–7.6) coated with ≈220 nm of indium tin oxide (ITO), a transparent conductor, on its outside surface which serves as the powered electrode while enabling optical access to the plasma. The packing material took up 22.5% of the total volume.

A second p-DBD system shown in Fig. 1b is a rectangular quartz (dielectric constant ε_r = 3.75–3.8) 100 mm tube with 1.5 mm thick walls having internal dimensions of 25 mm width, 90 mm length and a 10 mm gap where the plasma is generated. The rectangular quartz tube is terminated on both ends with quartz rectangular plugs having fittings for gas inlet and exhaust. The bottom plate (borosilicate glass, ε_r = 4.6) includes three dome structures having the same dimensions as in the first apparatus set on a ground plane consisting of copper tape. The structures accounted for 19.6% of the total reactor volume. The top powered electrode is also copper tape. This geometry is sufficiently similar to first that the plasma discharge formation mechanisms are essentially the same while also allowing for optical observations from the side. Combining the results from both systems then enables quasi-3-dimensional perspectives of discharge formation within a p-DBD.

Both configurations of the patterned DBD are simplifications of industrial scale PE-PBRs. These designs allow for improved optical access while their geometric simplicity makes them amenable to computations and model validation. However, these simplifications do have drawbacks. For instance, due to their random packing, commercial PE-PBRs have varying degrees of alignment between their dielectric beads and the applied electric field which impact the properties of the plasma. Different plasma phenomena may then occur simultaneously in different regions of a full-scale PE-PBR and interact, leading to more stochastic discharge behavior. The results presented here aim to elucidate

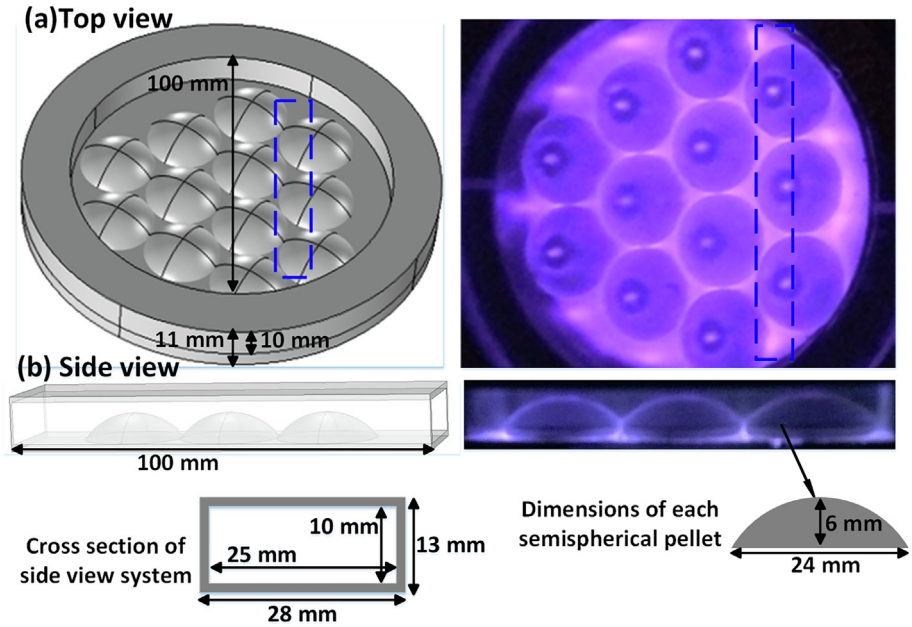

Fig. 1. Experimental setup with a patterned DBD. (left) Schematic and (right) CCD camera image of the (a) top view and (b) side view.

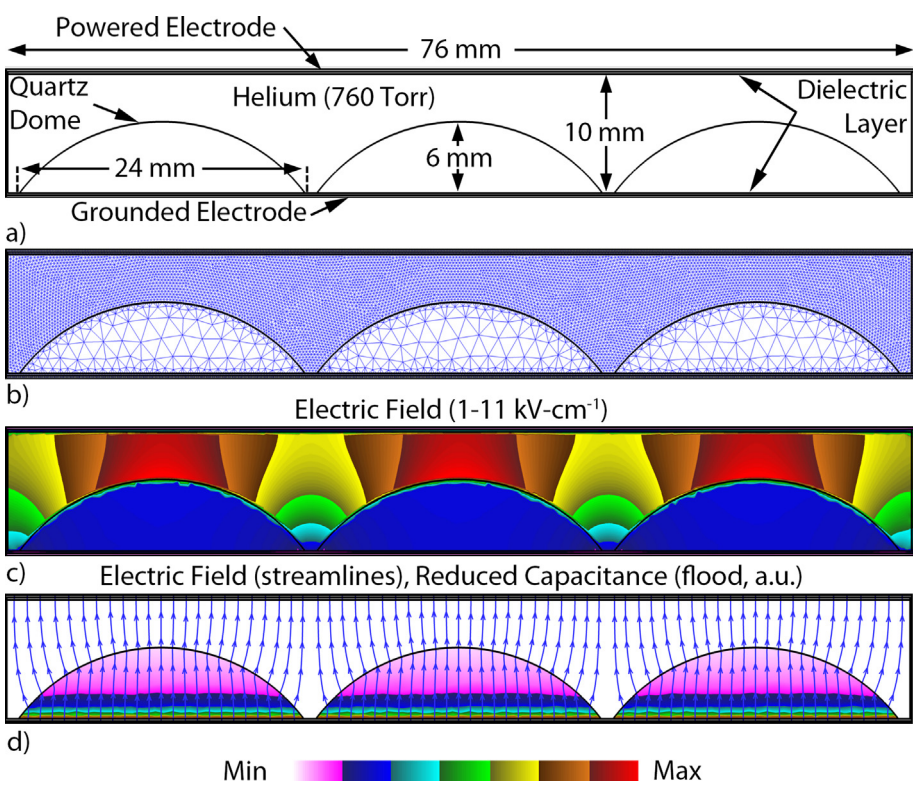

Fig. 2. Computational geometry. a) Schematic of the reactor having a height of 10 mm, width of 76 mm and a depth of 5 mm. Both electrodes are covered by a layer of dielectric 0.2 mm thick. b) Computational mesh. c) Electric field contours resulting from an applied voltage of 6 kV. The peak electric fields occur between the top dielectric layer and the apexes of the dielectric domes. d) Electric field streamlines along the surface of the dome and relative reduced capacitance. Angle between applied electric field vectors and surface of the dome decreases towards the contact points. Capacitance is lowest near the top of the domes.

basic plasma formation mechanisms which take place in PE-PBRs regardless of complexity.

Plasma is generated in helium gas (99.999% purity) having a flow rate of 2 slm (standard liters per minute), using a 10 kHz high voltage sinusoidal power supply. The plasma was imaged with an Andor ICCD camera through a 710 nm interference filter with a bandwidth of 10 nm to isolate the He 706.5 nm (He 3^3S to 3^3P) line dominantly populated by electron impact from the ground state. The threshold energy of He (3^3S_1) is greater than 21 eV. At atmospheric pressure, the effective lifetime of the emission is sufficiently shortened by collisional de-excitation that emission can be used as a measure of the rate of excitation. For this level, the excitation is almost all due to electron impact from the ground state and other mechanisms such as multi-step excitation from the metastable are small in comparison [23]. As a result, emission from He(3^3S_1) largely reflects the presence of energetic electrons at that time or position. The camera is phase synchronized with the power supply through an external pulse/delay generator and an internal delay generator to enable phase and space resolved optical emission spectroscopy (PROES) with 1 μs time resolution. Further details on PROES can be found in Refs. [24–26]. For the results in Fig. 7, no interference filter was used with a time integration of 0.1 μs and 0.5 μs steps between consecutive images.

3. Description of the model

The modeling was performed using the 2D plasma hydrodynamics simulator *nonPDPSIM* described in detail in Ref. [27]. Newton's method was used to implicitly and simultaneously integrate Poisson's equation and continuity equations for charged species over an unstructured, 2D numerical mesh. Charging of surfaces due to fluxes of ions and electrons was included in the electrostatic solution at each time-step while including secondary electron emission by ion impact with a coefficient of 0.1. The electron temperature was obtained from integration of the electron energy transport equation. Electron transport coefficient and rate coefficients as a function of electron temperature were obtained from a 2-term spherical harmonic solution of Boltzmann's equation for the electron energy distribution.

In this study, the initial background gas was pure helium at one atmosphere and 300 K. The reaction mechanism was a reduced form of that found in Ref. [27] and included 11 species (e^-, He^+, $He_2{}^+$, He and seven excited states of atomic and molecular helium) which resulted in 135 reactions. The computational geometry is shown in Fig. 2, and mirrors the second experimental geometry. Three 24 mm wide domes extend 6 mm into a 10 mm gas gap between two dielectric plates. The radius of curvature of the domes is 15 mm, separated at the apex by 24 mm. All dielectric materials had a permittivity of $\varepsilon_r = 4.0$ (quartz). This value is similar to the measured permittivity of the domes in the experiments ($\varepsilon_r = 4.6$), and the difference should not significantly impact the modeling results nor the validity of the comparison. The powered electrode was located at the top, while the bottom electrode was grounded. The width of the reactor was 76 mm, with dielectric covering both of its sides. Given the 2D geometry, the domes are functionally infinite rods perpendicular to the image in Fig. 2. These rods intrinsically have less electric field enhancement at their apexes compared to the 3-dimensional semi-spheres used in the experiments. For all calculations of volumetric energy deposition we assumed a reactor depth of 0.5 cm. The computational mesh included 9241 nodes with 6834 nodes located in the plasma region. The size of mesh cells varied between 0.2 mm near the surfaces of the dielectric to 1.8 mm at the center of the domes.

The study included a parameter sweep of positive and negative (± 5 kV to ± 8 kV) 200-nanosecond DC pulses, representing the individual current peaks observed in the experiments. The voltages used in the computations were higher than those in the experiments to compensate for the 3-dimensional electric field enhancement in the experiments that occurs above the domes and inside streamer heads. To initialize the discharges and to account for residual ionization left from previous discharge pulses, a uniform background pre-ionization of $1 \times 10^6\ cm^{-3}$ was used.

4. Experimental imaging of discharges in the p-DBD

In this section, we discuss results from experimental ICCD imaging of discharges in the p-DBD. Time-averaged, and space-resolved images of the discharge for applied voltage amplitudes V_p of 1.9 kV, 2.25 kV, 2.7 kV and 3.8 kV in the first geometry are shown in Fig. 3. These voltages were selected to observe transitions between specific phenomena. At a low applied voltage (1.9 kV, Fig. 3a), the plasma forms only at the center and apex of each dielectric semi-sphere where the gas gap is smallest and electric field is most intense. For an applied voltage of 2.25 kV (Fig. 3b), the most intense optical emission occurs at the apex of the domes and the contact points at the periphery of the domes. For the higher applied voltage of 2.7 kV (Fig. 3c), emission is marginally produced at the apex of the domes, but is most intense at the –contact points at the base of the domes. At the highest applied voltage of 3.8 kV (Fig. 3d), the optical emission is dominated by excitation occurring at the contact points at the base of the domes. The lack of observed visible emission along the surface and apex of the domes is largely due to the high intensity at the base of the domes that tends to saturate the camera sensor.

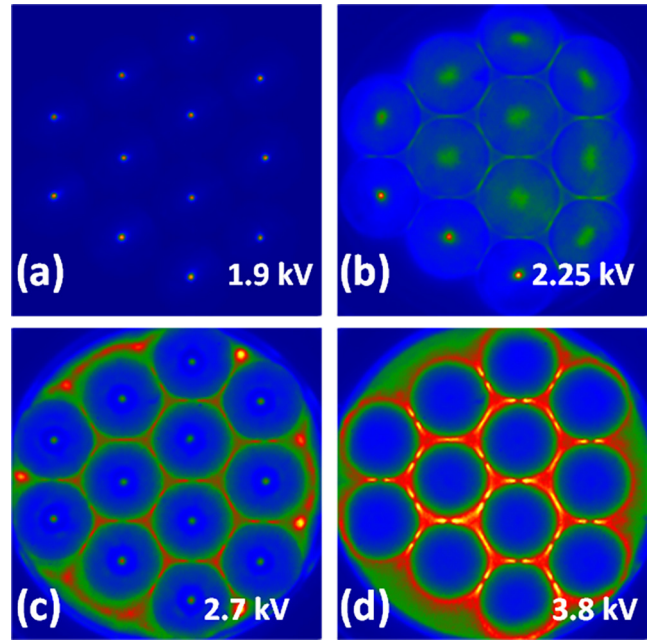

Fig. 3. Time averaged and space resolved images of the p-DBD at applied voltage amplitudes V_p of a) 1.9 kV, b) 2.25 kV, c) 2.7 kV and d) 3.8 kV.

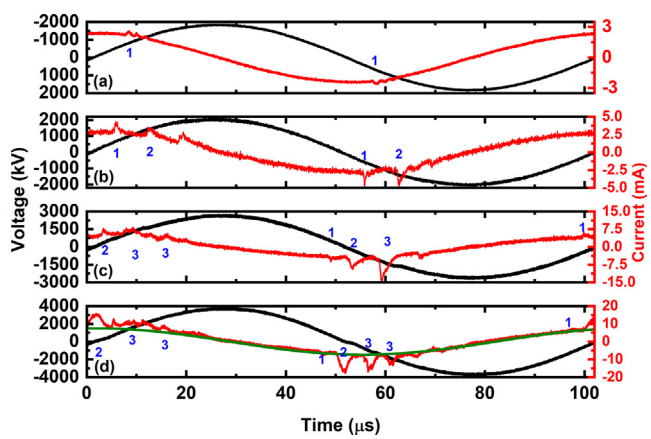

Fig. 4. Voltage and current waveforms of a p-DBD operated in helium, at a peak-to-peak applied voltage of (top-to-bottom) 1.9, 2.25, 2.7 and 3.8 kV. Sinusoidal waveform with no discharge current profile is shown in green in d). (For interpretation of the references to colour in this figure legend, the reader is referred to the web version of this article.)

Typical discharge current waveforms for different applied voltage amplitudes (V_p of 1.9, 2.25, 2.7 and 3.8 kV), are shown in Fig. 4. The voltage and current waveforms are typical for DBDs - the conduction discharge current appears when the applied voltage exceeds onset values towards the maxima of the positive or negative phases. The current pulses are labelled 1, 2 or 3, referring to the three discharge types observed and discussed below. The discharge current has a sinusoidal waveform with a few peaks during each half cycle. The sinusoidal part is largely due to the displacement current of the system, although there is a weak background ionization that persists from pulse to pulse [28,29]. The sharp peaks in the current profile indicate the discharge current. The amplitude and number of discharge current peaks increase with V_p while also occurring earlier. Note that the current scales were varied as the voltage increased to account for higher discharge current peaks.

The PROES measurements as a function of time were performed over the region shown by the blue box in Fig. 1a, with the results shown

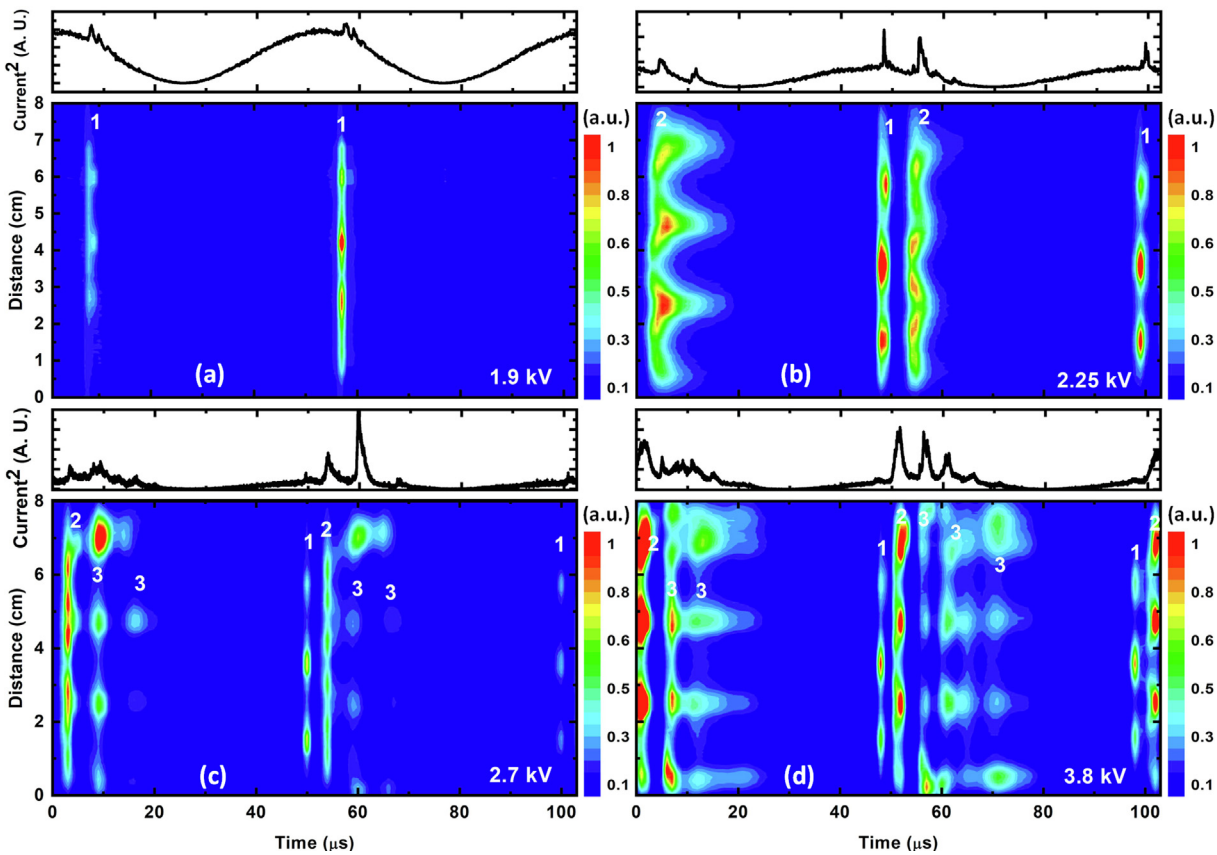

Fig. 5. Time resolved variation of the (top) square of the current and (bottom) axial emission from the He (3^3S_1) state for voltage amplitudes of (a) 1.9 kV, (b) 2.25 kV, (c) 2.7 kV and (d) 3.8 kV. The corresponding 2D emission images are shown in Fig. 6.

in Fig. 5. The images in Fig. 5 were taken with different intensifier voltages and rescaled to enable the emission in the less bright locations to be clearly discerned. Therefore, the actual emission maxima between the images cannot be directly compared. The discharge phenomena remained largely unchanged from one sinusoidal period to the next, and so only one period is shown in Fig. 5. Space and time-resolved emissions are correlated with the 2D images of the plasma in Fig. 6. Each of the 2D emission images were also normalized, to enable the emission in less intense regions to be clearly shown. To interpret the images, the time resolved changes in the emission are provided by Fig. 5, and the plasma structure is indicated by Fig. 6.

The time-resolved emission from the discharge for applied voltage amplitude of ≈1.9 kV is shown in Fig. 5a. The vertical axis shows the distance (the vertical distance of the dotted rectangle in Fig. 1a), and the horizontal axis indicates the duration (≈102 μs), one complete cycle. The applied voltage amplitude of 1.9 kV is the lowest for which a uniform and stable plasma can be generated. The single emission structure (indicated as 1 in Fig. 5a) occurs during each half cycle for approximately 3–5 μs and there is no observable emission for the rest of the cycle. Overall, at the lowest voltage, the plasma is generated for only ≈3–5 μs during the cycle. Axially, there are three emission maxima corresponding to the apex of the three dielectric domes. The square of the current [Fig. 5a (top)], is related to the power deposition and correlates well with the temporal maxima of emission [Fig. 5a (bottom)].

The images shown in Fig. 6a for an applied voltage of 1.9 kV indicate that in both halves of the cycle (i.e., t = 8 μs and 59 μs), the discharge is generated at the apex of each dielectric dome at the position of the minimum distance between the dome and top electrode. The discharge is terminated by charging of dielectrics as in conventional DBDs. The residual voltage left across the gap and the surface charging, which combined generate a parallel component of the electric field along the surface, is not sufficient to support a surface ionization wave (SIW) of significant magnitude. The outline (or surface) of the dome is visible in the images, however, with low emission intensity.

The space and time-resolved emission from the discharge for ≈2.25 kV amplitude is shown in Fig. 5b. Two emission structures form during each half of the voltage cycle, indicated by 1 and 2. Again, the axial emission (bottom) correlates well with the square of the current. The general behavior and structure of the discharge are similar during both halves of the cycle, but the peak current and the number of current peaks differ. The first emission structure in both halves (labeled 1) resembles that of the lower voltage, where there are three maxima occurring at the apex of the domes. Compared to the lower voltage, the emission intensity appears more homogenous.

The second peak in emission during both halves of the cycle (labeled 2) consists of emission propagating away from the apex of the domes. The emission structure has a ring-like shape propagating along the surface of the dome with increasing diameter until reaching the contact points at the base of the domes at ≈6 μs. At this time, the discharge brightens (ICCD counts increase ≈15%) at the contact point (at ≈9 μs) followed by dimming at ≈17 μs (ICCD counts decrease ≈78% compared to 9 μs). These images are likely explained by a surface ionization wave [11,20], where surface charging produces a tangential electric field which supports propagation of an ionization front. The speed of the SIW changes during the journey from the apex to the contact point which cannot be quantitatively determined with the current time resolution. Qualitatively, the speed of SIW is lowest at the apex of the dielectric structure. The speed of the SIW increases as it approaches the contact point.

The speed of the SIW is determined, in part, by how long it takes to charge the dielectric under the head of the SIW. In a conventional DBD with parallel plates, filamentary microdischarges (F-MDs) will be quenched if the dielectric underneath the streamer is fully charged

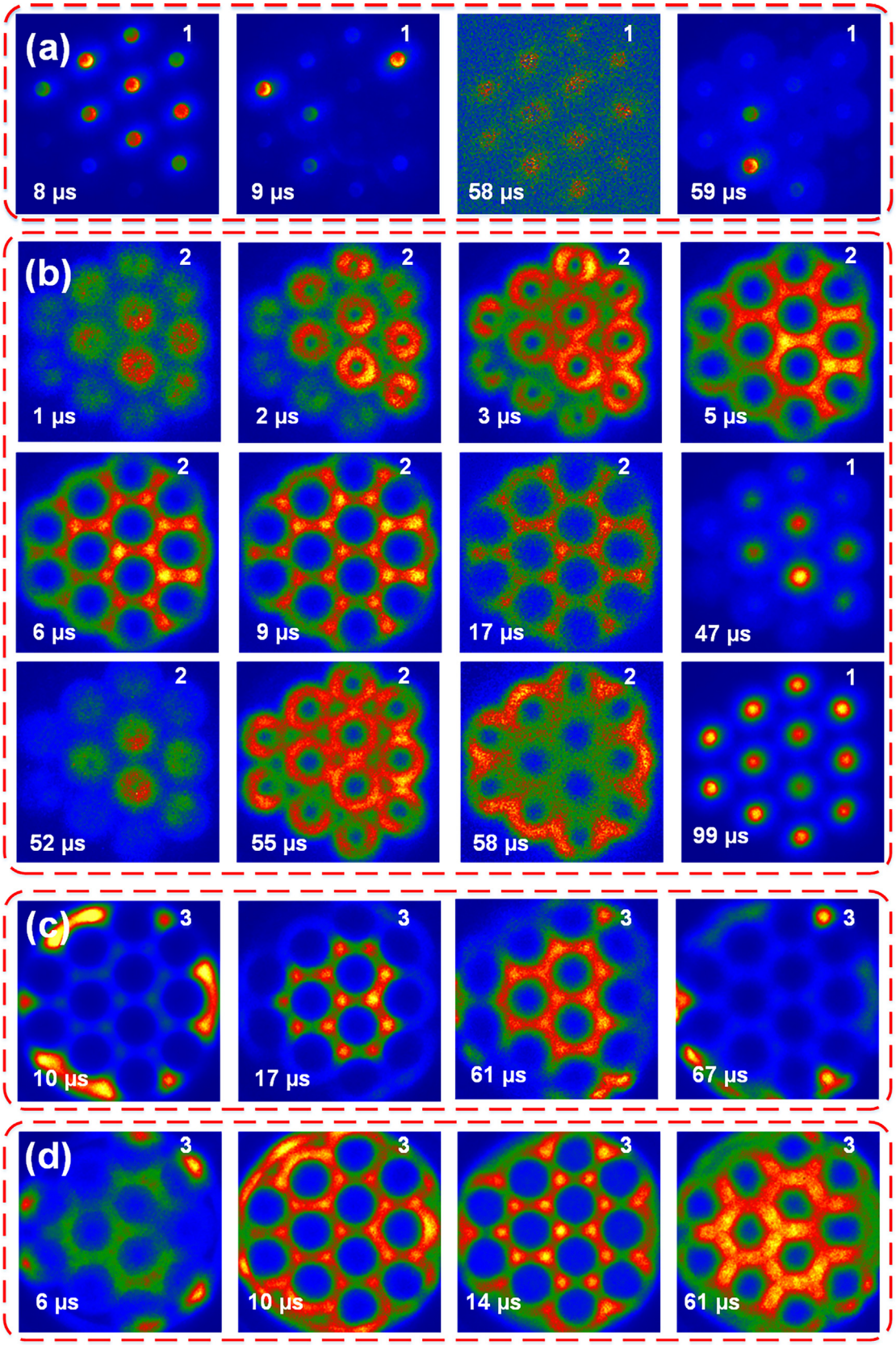

Fig. 6. Time-resolved images of the discharge for applied voltages of (a) 1.9 kV, (b) 2.25 kV, (c) 2.7 kV and (a) 3.8 kV. The corresponding time resolved axial emission is shown in Fig. 5.

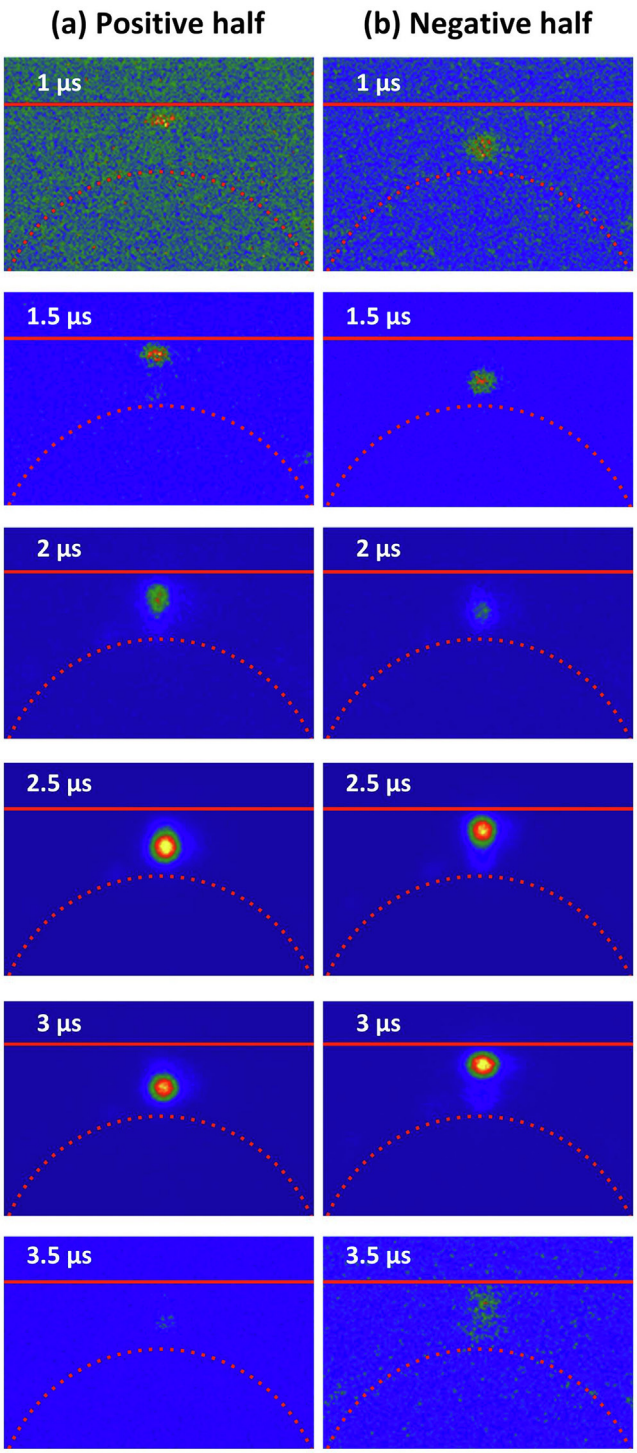

Fig. 7. Time-resolved images of total discharge emission in the (a) positive and (b) negative halves of the applied voltage for an amplitude of 1.5 kV. The images are recorded without interference filters with an integration time of 0.1 µs and a time shift of 0.5 µs between successive images. The dotted (curved) and solid (flat) red lines indicate approximate location of the dielectric surfaces. (For interpretation of the references to colour in this figure legend, the reader is referred to the web version of this article.)

depending on the specific capacitance of the dielectric - C_o (F/cm^2), capacitance per unit area of the dielectric material. In a conventional DBD, the C_o is essentially constant at all locations because the ratio of the dielectric constant of the material and its thickness is constant. In a patterned DBD, however, this capacitance varies laterally along the surface of the electrode since the effective thickness of the dielectric varies. This variation can be seen in Fig. 2d. The reduced capacitance was calculated as $C_0 = \varepsilon_r/d$, where ε_r is the permittivity of the domes, and d is the distance from the surface of the dome to the bottom electrode. This means that the amount of surface charging also varies as a function of position. The C_o is smaller at the apex of the dielectric structure and larger near the contact point, because the dielectric thickness is larger at the center and smaller near the contact point. On this basis, the SIW would be expected to propagate faster near the apex of the dielectric structure and slower near the contact point due to the increase in C_o. However, we observe the opposite trend – the SIWs propagate faster as they move toward the contact point.

This phenomenon can be explained by the direction of the electric field at the tip of the ionization wave. In the absence of plasma, the electric field would be directed from the anode and toward the cathode – perpendicular to the surface at the top of the domes, and nearly parallel to the surface near the contact points. This dependence is shown in Fig. 2d as streamlines of the electric field vectors. When the SIWs first form near the apex, they experience little or no external electric field parallel to the surface. However, as the ionization fronts propagate along the hemi-spherical surfaces, the external electric field begins to increasingly point in their direction of travel which causes the SIWs to accelerate. It appears for these conditions that the speed of the SIW is more sensitive to the parallel component of the electric field than C_o.

The emission during the second half of the cycle (with the opposite polarity) generally has a similar ring-like structure as during the first half. There are SIWs generated at 52, 55 and 58 µs. The SIW structure is dissimilar during the two halves. This is because during one half of the cycle the propagation is over the flat dielectric while during the other half, it is over the curved dielectric. This implies that the SIW travels a longer distance during the positive half over the dome and shorter distance during the negative half in this configuration. Also, the effect of C_o will not be important during the negative half when the SIW travels over the flat dielectric.

The discharge with a bias of 2.7 kV generates a larger number of current peaks and emission structures during each half of the voltage cycle compared to the lower voltage. The duration of the SIW decreases with the increase in applied voltage. The capacitance of the dome is constant while the current density increases with increasing voltage. This leads to a more rapid charging of the surface, which produces the tangential components of the electric field that sustains the SIW, resulting in a higher propagation speed.

Following the SIWs reaching the contact points, several successive emission structures were observed, which are labeled 3. The 2D images indicate intense plasma generation at the contact points ranging from 17 µs to 61 µs. This emission corresponds to the timing of the current peaks. Other peaks in current, however, do not exactly correlate with the axial emission as the plasma is generated at the edges of reactor (Fig. 6b, t = 10 µs and 67 µs) which is outside the region recorded by the ICCD. The current peaks at ≈10 µs and 67 µs have the highest amplitude (compared to S-MDs on similar half cycle ≈120 and 200%, respectively), which indicates that at moderate voltages edge effects play an important role.

The time resolved emission for an applied voltage ≈3.8 kV is shown in Fig. 5d. The first two peaks in each half cycle show discharge structures similar to those observed at lower voltages. The second peak in each half of the cycle (t ≈ 51 µs and 102 µs) is produced by the SIWs and has the highest intensity (up to ≈9 times the ICCD count compared to F-MD). Due to their high speed of propagation, the SIW quickly reach the contact points between the domes. The current peaks dominantly generate emission at the contact points (≈10, 14 and 61 µs) or edges (≈6 µs). This likely results from the thickness of the bottom dielectric being smallest in these regions, leading to increased capacitance. The larger capacitance enables a larger fluence of current to the surface at those locations prior to the dielectric fully charging and the

microdischarges extinguishing. Compared to the lower voltages, the discharge here is more uniform and covers most of the contact points, indicating that the S-MDs dominate.

2D images of the total emission viewed from the side (as shown in Figs. 1b and 2) during the positive and negative cycles are shown in Fig. 7. Due to changes in geometry, the minimum voltage required for breakdown in this configuration was lower, and plasma was produced at 1.5 kV. These images were recorded without interference filters due to the low emission intensity. The integration time is 0.1 μs with a time shift of 0.5 μs between successive images. The shorter integration time was selected in order to better resolve the transients.

During the positive portion of the cycle, emission first occurs (at t = 1 μs) in front of the anode, which is followed by a positive streamer being initiated near the flat dielectric and moving towards the cathode at the bottom. When the streamer reaches the top of the dome at 2 μs, it begins to charge the dielectric surface [maximum ICCD count (MIC) ≈ 10,000]. The plasma which resulted from the propagation of the streamer is the F-MD in the gap, observed at 2.5 μs (MIC ≈ 12,000). As the surface of the dome charges, the potential drop between the dielectrics decreases and ionization in the gas gap ceases. This then leads to a decrease in the intensity of emission at 3 μs (MIC ≈1400), and the F-MD dissipates at 3.5 μs. During the negative half cycle, similar behavior is observed. However, now a negative streamer is initiated near the apex of the dielectric and is directed towards the anode at the top. This sequence of events is typical of DBDs [30] regardless of packing geometry. However, in the packed DBD the F-MD is preferentially generated at the location of the minimum gap. When the gaps at different locations have the same dimension, multiple F-MDs are synchronized in time.

Images of He(3^3S_1) emission observed in the side geometry for positive and negative half cycles at an applied voltage amplitude of 3 kV are shown in Figs. 8 and 9, respectively. In both cases, the images were recorded for an integration time of 1 μs and step size of 1 μs between successive images. Each image is tagged with one of the three mechanisms: 1 – Positive streamer (PS) and Filamentary microdischarge (F-MD), 2 – Surface ionization waves (SIWs), and 3 – Surface microdischarges (S-MDs). As for the case with an applied voltage of 1.5 kV, the initiating discharge during the positive half cycle is a cathode-directed streamer originating at the top dielectric and propagating downwards towards the apex of the domes. By 3 μs, the filamentary microdischarge is fully formed (MIC ≈ 6000). The successive images from 4 μs to 10 μs show the generation of the SIWs which accelerate from the apex of the dielectric dome towards the contact points at their base. The MIC ≈ 7000 at 4 μs, which decreases to ≈1900 at 5 μs, and later increases to ≈10,000 at 8 μs. The MIC is consistent with the SIW decelerating during the initial journey and later accelerating closer to the contact point. At 11 μs, the SIW propagating on the surface of adjacent domes merge prior to reaching the contact points. This is similar to the image from the top in Fig. 6b at 14 μs. Finally, the SIWs reach the contact points at 12 μs and a higher density plasma occurs in the form of a surface microdischarge [similar to 15 μs and 18 μs in Fig. 6b]. In addition to the SIWs on the domes, weaker emission occurs from SIWs on the flat dielectric (indicated by arrows). The intensities are MIC of ≈1700 at the flat dielectric compared to ≈10,000 at the dome for the image at 8 μs. These SIWs also move away from the apex of the domes.

When the SIWs reach the contact points between the domes in the positive cycle, several additional pulses of emission occur, indicated in Fig. 9 as mechanism 3. This emission is produced by surface-microdischarges (S-MD) at the contact point (such as at 24 μs) or a filamentary microdischarge (F-MD) in the volume (more intense at the edges) such as at 16 μs (MIC ≈24,000). Due to the high capacitance of the dielectric in the region of the contact-points, the discharge can be sustained for many microseconds before the dielectric is fully charged, as shown by the emission between t = 12 μs and t = 24 μs in Fig. 8.

The optical emission during the negative half-cycle (Fig. 9) is similar to that during the positive half-cycle with the direction of propagation being reversed. Here, the cathode directed streamer propagates from the surfaces of the domes towards the flat dielectric. At 5 μs, a filamentary microdischarge occurs. The successive images from 6 μs to 12 μs show the generation of SIWs on the flat dielectric surface beginning directly above the apex of the domes. The SIWs propagate radially outward until SIWs from adjacent domes merge at the location axially opposite the contact points at 14 μs. (The merging corresponds to the image from the top in Fig. 6b at 64 μs). In addition to the SIWs propagating on the flat dielectric, there is some weak emission at the surface of the curved dielectric (indicated by arrows), resulting from SIWS which also move towards the contact points. Following their merging, there are successive pulses of emission at 14 μs and 20 μs, which is again similar to mechanism 3 from the top view.

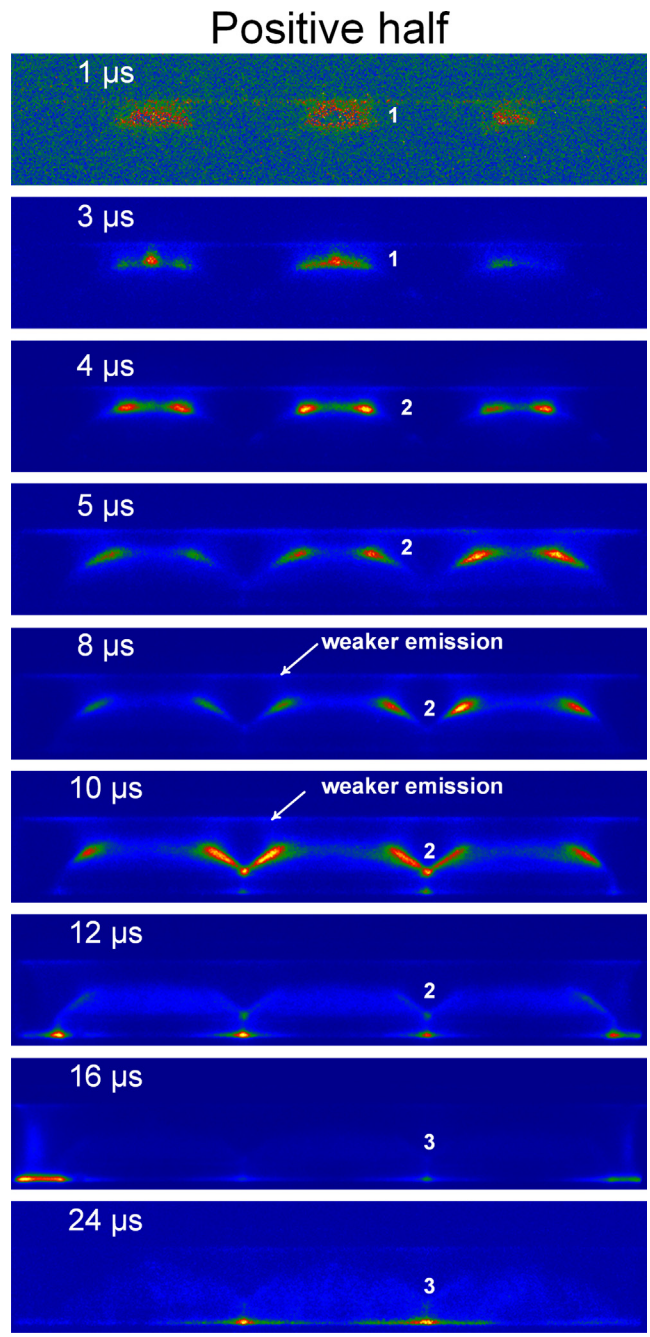

Fig. 8. Time-resolved images of He (3^3S_1) emission for the positive half cycle for an applied voltage amplitude of 3 kV. The images are recorded with an integration time and time shift of 1 μs.

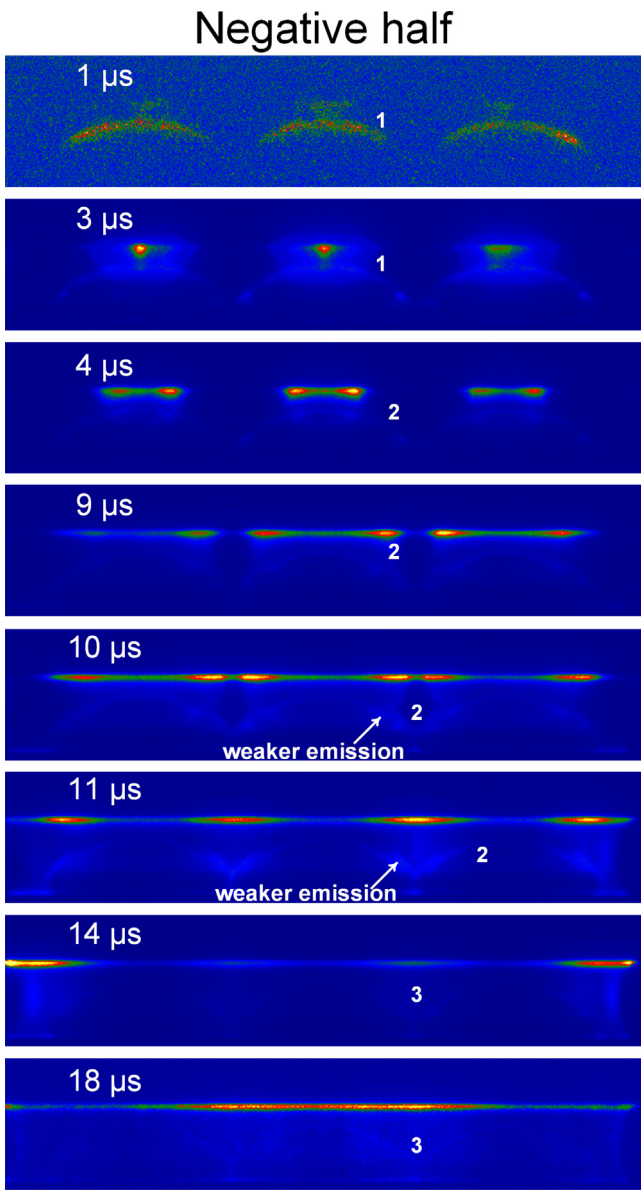

Fig. 9. Time-resolved images of the He (3^3S_1) emission for the negative half cycle, for an applied voltage amplitude of 3 kV. The images are recorded with an integration time and time shift of 1 μs.

These results can be summarized as follows. Multiple current peaks occur in each half cycle which produce short discharges and pulses of optical emission. The number of discharge pulses increases with increasing voltage. The peaks in the current correlate well with the time and space resolved optical emission. Increasing voltage initiates the discharges earlier, with the first current peaks manifesting themselves as F-MDs initiated as a cathode directed positive streamer. At the lowest voltage which has a single current peak, only F-MDs are generated at the apex of each dome. With increasing voltage, a second peak in current occurs, and SIWs are generated over the flat topp dielectric during the negative cycle and over the curved dielectric of the domes during the positive cycle. The SIWs from adjacent domes propagate towards each other and eventually merge with speeds that increase with increasing voltage.

Similar trends in the evolution of plasma formation mechanisms were observed experimentally by Butterwroth et al. [19]. The authors used a single dielectric bead to study the impact of dielectric constant and applied voltage on plasma propagation. As the voltage was increased, they observed formation of Townsend avalanches, microdischarges and surface streamers. Van Lear et al. performed a computational investigation of a 2-bead PBR. [9]. They found that the plasma was initiated at the points of greatest field enhancement regardless of voltage. However, as the peak-to-peak potential increased from 4 kV to 7.5 kV, a transition from microdischarge-like plasma to a surface-dominated discharge took place.

With positive polarity, the merging that occurs at the contact points of adjacent domes produces bright emission, which is enabled by the high capacitance at those points. SIWs produce the brightest optical emission as well as the highest peak current, consistent with previous observations [11].

5. Simulations of discharges in the domed structures

The base case for the 2D modeling uses a 200 ns voltage pulse of +6 kV, with a 5 ns rise time and a 5 ns fall time, followed by 600 ns of a voltage-off period. With the simulations being performed in 2-dimensions, higher voltages are required to reproduce the same phenomena as in the experiments. This disparity in voltage is due to the larger electric enhancement that occurs at the apexes of the 3-dimensional semi-spherical domes and hemispherical ionization fronts in the experiment compared to the 2-dimensional representation of these structures as cylinders or rods in the model. Although the majority of the experimental phenomena are reproduced and explained by the model, the applied voltages at which these phenomena occur are larger in the model, which then reduces their timescale.

The electron impact ionization source term and electron density during the base case discharge are shown in Fig. 10. As a positive potential is applied to the top electrode, electrons quickly respond to the electric field, drift upwards, and deposit charge on the top dielectric. Heavy ions are left behind in the gas-gap, resulting in formation of positive space-charge with a peak positive density of 3.7 nC-cm^{-3}. The production of positive charge enables formation of positive streamers between each of the domes and the top dielectric, shown at t = 35 ns in Fig. 10a and t = 37 ns in Fig. 10b. The electrons in the streamer head have temperatures of $T_e \approx 6.0$ eV, resulting in electron impact ionization peaking at $S_{\text{e-impact}} \approx 1 \times 10^{20}$ cm^{-3}-s^{-1}. Once the streamers breach the gas gap, micro-discharges form (Fig. 10b, t = 62 ns). Filamentary microdischarges between the domes and the top dielectric are the initiating discharges seen in experimental results in Fig. 5, Fig. 6(a)–(b), Fig. 7a and Fig. 8; and identified as 1. Once plasma forms in these regions the high conductivity reduces the E/N (electric field/gas number density) which produces lower electron temperatures (0.1 eV ≤ T_e ≤ 4.3 eV). The electron-impact ionization in the region largely ceases (-1.6×10^{20} cm^{-3}-s^{-1} ≤ $S_{\text{e-impact}}$ ≤ 1.8×10^{17} cm^{-3}-s^{-1}), and only remnant plasma remains, shown in Fig. 10a, t = 60 ns.

As plasma charges the dielectric domes, electric fields parallel to the surface form, leading to development of surface ionization waves (SIWs), shown at t = 60 ns and 62 ns in Fig. 10. The electrons in the ionization fronts of the SIWs have electron temperatures peaking at 7.3 eV, which lead to high rates of ionization (6×10^{22} cm^{-3}-s^{-1}), as well as high densities of excited and light-emitting species (2×10^{16} cm^{-3}). This stage of the discharge corresponds to that identified as 2 in Fig. 9 (from the side) at 5 μs and as rings expanding around the domes in Fig. 6b (from the top) at 11 μs. While light emitting species are still present in the bulk plasma, their densities are 3 orders of magnitude lower than those in the SIW fronts near the surfaces, and so emission from the SIWs dominates. As the SIWs spread, ionization in the bulk gas ceases (Fig. 10a at t = 189 ns) as the high conductivity plasma in the bulk plasma lowers the local E/N. As in the experiments, the SIWs across the domes merge at the contact points where the highest electron density occurs, 6×10^{15} cm^{-3}. The thinness of the dielectric in these regions produces high capacitance which supports a high surface charge density (peaking at 20.4 nC-cm^{-2}). These computed results correspond well with the experimental results shown in Fig. 8, where the brightest optical emission occurs from contact points

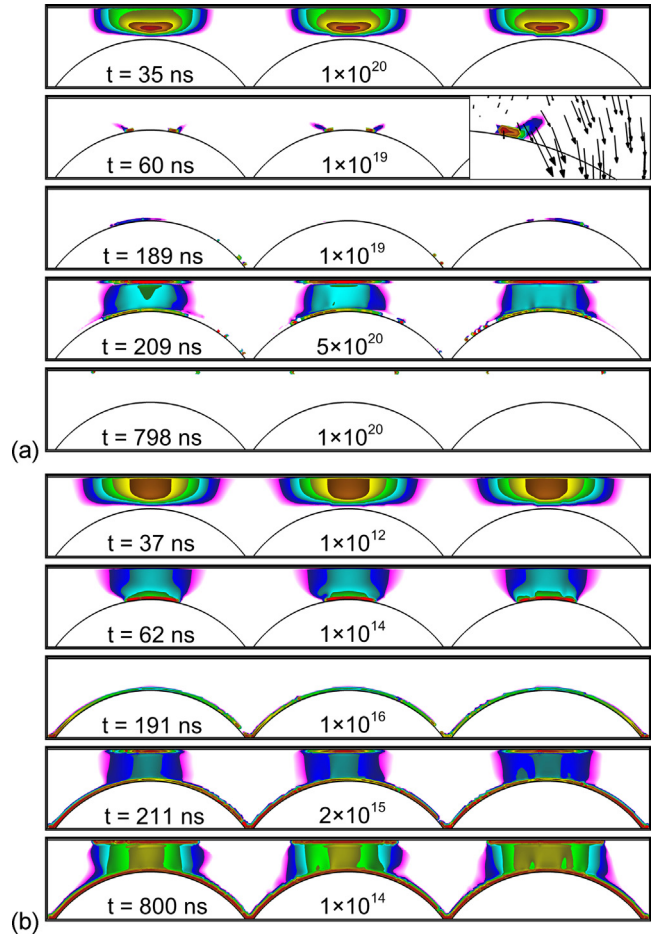

Fig. 10. Evolution of a) electron impact ionization source and b) electron density during the discharge in the base case (+6 kV) displayed using log scales. Times and peak plotted values are noted in the figures.

between domes when SIWs merge. With the voltage pulse ending at t = 205 ns, the charge deposited on the dielectric leads to restrikes, as is shown in Fig. 10a at t = 209 ns, and an increase in the electron density in the microdischarges shown in Fig. 10b at t = 211 ns. While not shown in Fig. 8, this process also occurs in the experiments when the polarity of the voltage is reversed. In Fig. 6b, for example, the S-MDs at t = 26 µs transition into F-MDs at t = 56 µs due to the same restrike phenomenon.

The base case was repeated with the positive voltage varied between + 4 kV and + 8 kV. No breakdown occurred at + 4 kV. At V = +5 kV, only microdischarges developed at the apex of the domes shown in Fig. 11a. These structures are similar to the experimental trends observed from the top at V_p = 1.9 kV (Fig. 6a) and from the side at V = 1.5 kV (Fig. 7a). While SIWs begin to form, the plasma densities in the F-MDs are relatively low (peak $n_e \approx 5 \times 10^{13}$ cm^{-3}), leading to a low rate of charging of the dielectric domes (peaking at 5.9 nC-cm^{-2} at the end of the pulse – approximately 5 times lower than in the + 6 kV base case). This low rate of surface charging did not produce a large enough parallel component of the electric field (peaking at 13.2 kV/cm) to support propagation of SIWs while the voltage was on.

Discharges at higher voltages (V_p = +7 kV and + 8 kV) generally followed the same sequence of plasma structures as the base case, and so only the results for V_p = +8 kV will be discussed in detail. (See Fig. 12.) The discharge was initiated by a positive streamer beginning on axis above the apex of each dome, which evolved into a F-MD. However, due to higher applied voltage, the electron temperatures in the streamer head were larger ($T_e \approx 6.8$ eV compared to 6.0 eV for the base case) and the resulting electron densities doubled from the base case value of 8.0×10^{11} cm^{-3} to 1.6×10^{12} cm^{-3}. The time required for the plasma to breach the gas gap decreased from approximately 41 ns to 18 ns. Similar behavior was observed in experimentally measured discharge current (Fig. 4) and space resolved emission (Fig. 5), where with an increase in applied voltage from 1.9 to 3.8 kV, the F-MD initiated ≈10 µs earlier. The increases in energies and densities enable the SIWs to develop and propagate more quickly.

With an applied voltage of + 8 kV, plasma nearly fully covers the domes by t = 50 ns, as shown in Fig. 12. As the surface of the dome charges, the potential lines are bent (Fig. 12b), leading to electric field enhancement and larger E/N, which supports an electron temperature $T_e \approx 8.5$ eV, and electron impact ionization source peaking at $S_{e\text{-impact}} \approx 1 \times 10^{25}$ cm^{-3}-s^{-1} in the head of the SIW. Due to the resulting high electron densities (peaking at 1×10^{16} cm^{-3}, Fig. 12c) when the SIWs reach the contact points between the domes, the capacitance of the surface is quickly charged, and the discharge extinguishes. This sequence is not observed experimentally, likely due to the applied voltage being lower. In the model, once the capacitance of the contact points was fully charged, plasma acted as a conductive sheet on top of the domes. At this time, the potential at the top of the domes becomes nearly equal to the potential at the contact points. This equality leads to an increase in electric field and ionization rate in the bulk plasma shown in Fig. 12b and 12e, where electron impact ionization sources are shown directly before and after the SIWs merge. As a result, a short-lived burst in bulk ionization took place (Fig. 12e).

The voltage sweep was also performed for negative polarity (−4 kV to −8 kV). No discharge occurred at −4 kV as this voltage is lower than the breakdown field of helium. At −5 kV, only the F-MD formed, as shown in Fig. 11b. The discharge evolution for −6 kV is shown in Fig. 13 in the same format as the positive voltage base case. In a similar fashion to positive polarity, the discharge begins with electrons moving away from the cathode and charging the dielectric domes. A positive streamer developed as positive space-charge was left behind in the gas-gap (shown in Fig. 13 at t = 35 ns and 37 ns). The resulting micro-discharge was more diffuse than those at + 6 kV, which is typical of negative discharges [31]. As the microdischarges charged the top dielectric, surface ionization waves formed (Fig. 13 t = 83 ns and 85 ns). The structure is similar to the experimental results observed from the side in Fig. 9, at 4, 9 and 10 µs. The SIWs over the top dielectric were less intense ($S_{e\text{-impact}} = 1.6 \times 10^{19}$ cm^{-3}-s^{-1}) than those on the surfaces of the domes (8.3×10^{21} cm^{-3}-s^{-1}) due to the topology. The top dielectric surface is perpendicular to the applied electric field, requiring that parallel electric fields to sustain SIWs be produced dominantly by surface charging. The electric field at the surface of the domes has a component parallel to the surface, which enhances initiation and propagation of SIWs.

In the negative voltage base case, electrons spread across the surfaces of the domes, but their density is relatively low, peaking at $n_e \approx 5 \times 10^{12}$ cm^{-3} (Fig. 13 at t = 149 ns and 150 ns). The electrons along the surface were not self-propagating ionization fronts; but are rather due to electron transport along the electric field lines. The surfaces of the domes charged to −9 nC-cm^{-2}, while the top dielectric reached +34 nC-cm^{-2}. Once the applied voltage was turned off, this surface charge resulted in a peak electric field of ≈16 kV-cm^{-1} which was sufficient for breakdown and the formation of a restrike, as shown in Fig. 13 at t = 205 ns and 210 ns. These trends are similar to the experimental results in Fig. 9 (negative half) at 14 and 18 µs. The difference in location of the restrikes between the model and experiment could be explained by the fact that in the experiment the SIWs over the flat dielectric merge at a location above the contact point. The F-MD or re-strike occurs at the same location. However, in the simulation during this time, the SIWs from the two sides do not merge together and therefore the restrike is near the center of dielectric structures.

In general, increasing the magnitude of the voltage resulted in similar trends, regardless of polarity. The evolution of E/N, electron impact ionization source term with equipotential lines and electron

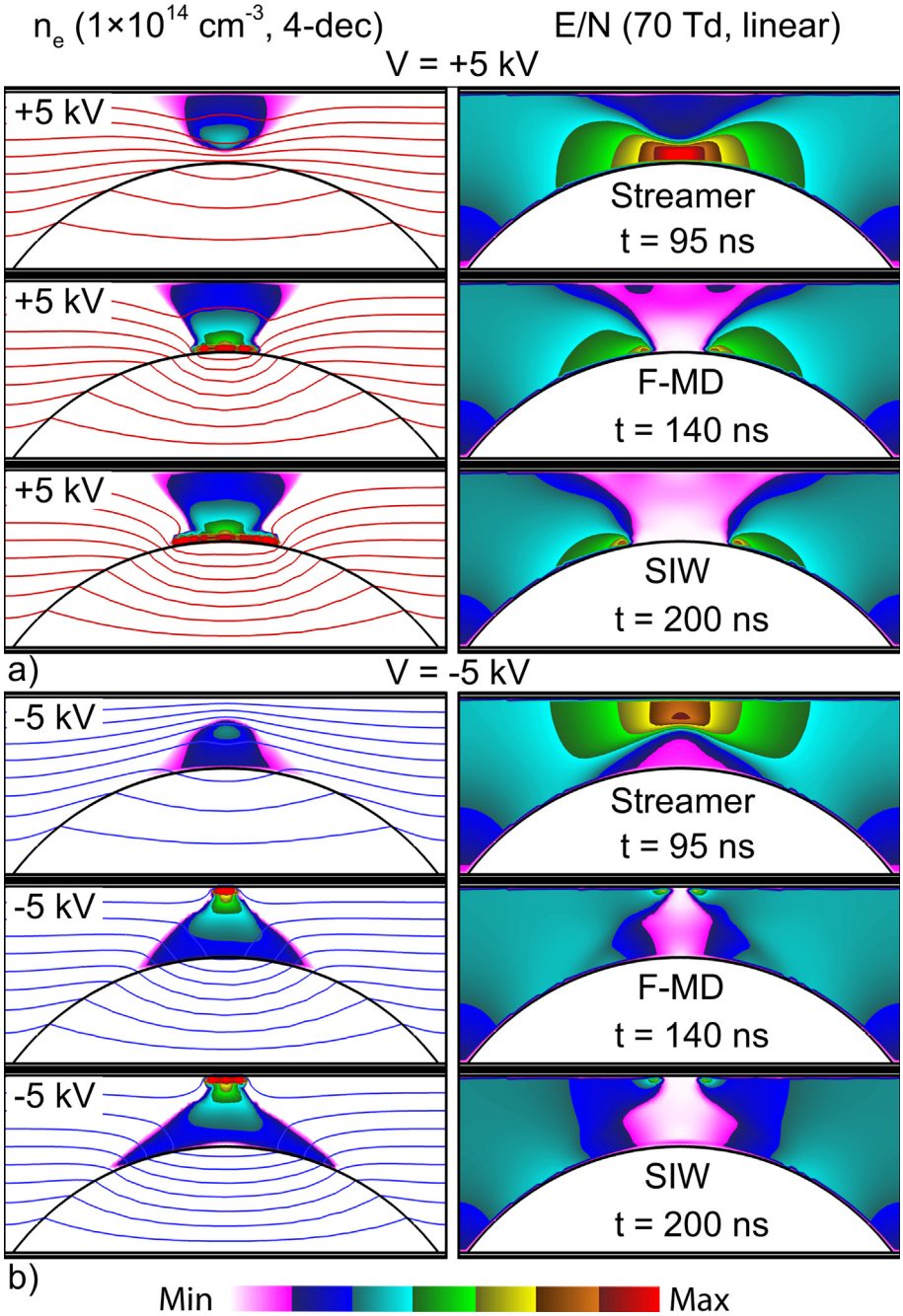

Fig. 11. Evolution of electron density, equipotential lines (left) and reduced electric field (right) for a) + 5 kV and b) −5 kV voltage pulses. Formation of positive streamers, filamentary micro-discharges and surface ionization waves are shown at times noted in the figure. Each equipotential line represents a potential change of 500 V. Electron densities are plotted on a log-scale.

density are shown for −8 kV in Fig. 14. Following the initial upward-directed positive streamer, plasma spreads across the domes, while an intense SIW propagates along the top dielectric (Fig. 14b and 14c). Since the electrons near the domes follow the electric field lines, a region of low electron density ($\approx 10^{11}$ cm^{-3}) forms at the top of the domes, (Fig. 14f). The plasma here is less conductive than with the positive polarity pulse. As a result, the potential does not redistribute, and the burst of ionization which occurs with + 8 kV does not form. This sequence is shown in Fig. 14e.

The sums of the densities of species which emit in the visible spectrum at t = 800 ns are shown in Fig. 15 for each of the applied voltages. These states include He(3P), He(3S), and He(2^1P). At ± 5 kV, only a microdischarge between the domes and the top dielectric formed. Surface ionization waves formed, but the pulse length was too short to allow for their propagation along the entirety of the dielectric. At higher voltage magnitudes, plasma covered the entirety of the domes, and the highest densities of light-emitting species were at the top dielectric layer during negative pulses [Fig. 15(a)–(d)] and at contact points between the domes when the applied voltage was positive [Fig. 15(e)–(h)]. The highest densities of excited He species occurred at +8 kV, with peak value of 6.9×10^{14} cm^{-3} at t = 55 ns, which then decreased to 3.7×10^{12} cm^{-3} at t = 800 ns. Of the light-emitting species, He(2^1P) and He(3P) had the highest densities, peaking at 2.7×10^{14} cm^{-3} and 3.7×10^{14} cm^{-3}, respectively, at t = 55 ns. Their densities decreased to 3.6×10^{12} cm^{-3} and 6.0×10^{12} cm^{-3} at t = 800 ns, indicating that the He(3P) state is the main source of visible

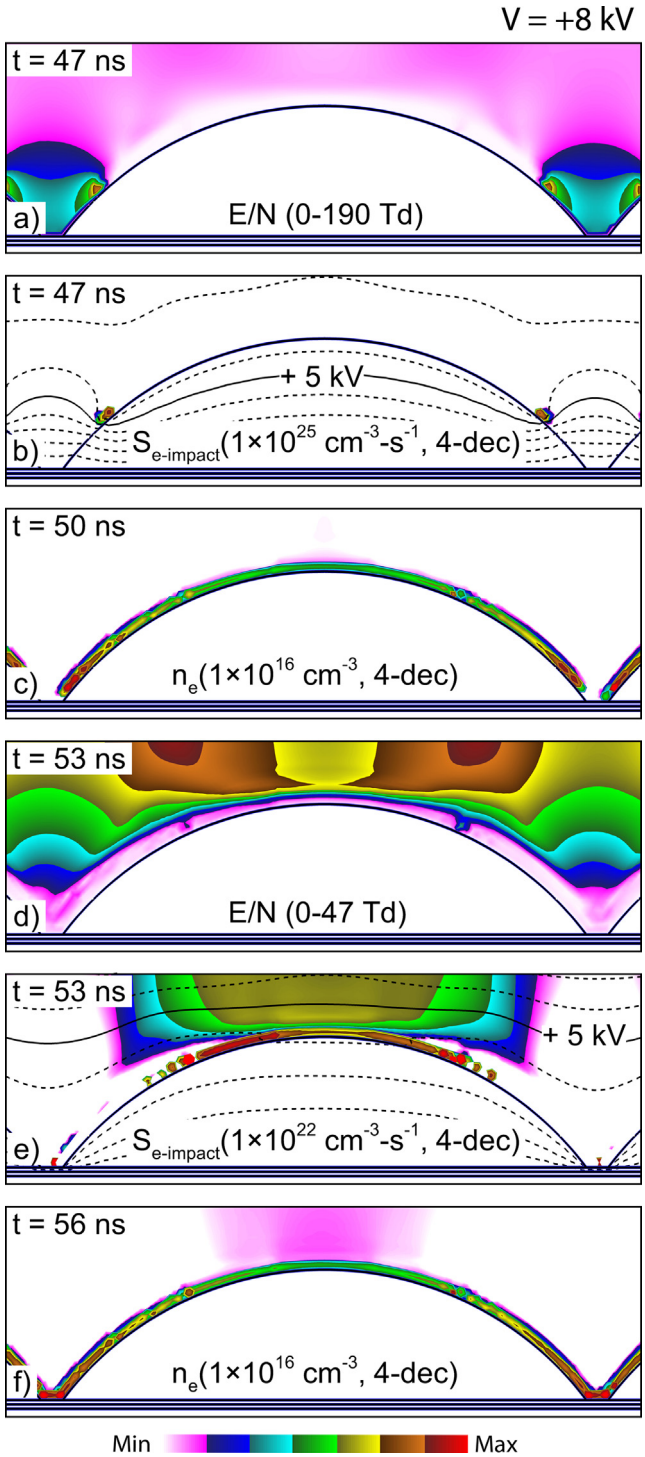

Fig. 12. Reduced electric field (E/N), electron impact ionization source term, electron density for +8 kV applied voltage. Electric potential lines are overlaid on electron impact ionization source term contour plots, with each line representing a 1 kV change. Times and peak plotted values are noted in the figures.

light.

The structure of the plasma also varies as the polarity reverses at a given voltage amplitude. When the applied voltage is negative the plasma is largely diffuse and fills a greater fraction of the volume of the reactor. However, the peak densities of light-emitting species, are greater during a positive-polarity pulse. These trends are due to the topology of the dielectric with respect to the applied electric field. The

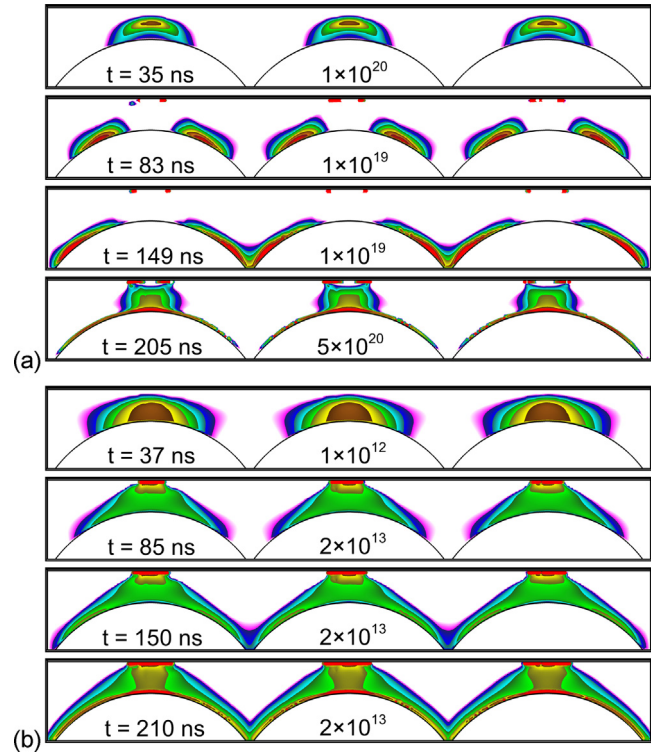

Fig. 13. Evolution of a) electron impact ionization source term and b) electron density during the discharge in the negative base case (−6 kV). Times and peak plotted values are noted in the figures. Log scales.

curvature of the domes enables the applied electric field to have components parallel to the surface. When the applied voltage is negative, the direction of the vector electric field enables electrons to drift downward and along the curvature of the domes, diffusing into regions further away from the initiating microdischarge. Conversely, during a positive polarity pulse, the electrons move towards the flat dielectric layer at the top of the reactor and the plasma remains more compact.

In summary, the simulation produced qualitatively similar phenomena to the experiment. Experiments and simulations indicate that the discharge is sustained first by F-MDs, followed by the SIWs and S-MDs at the contact points and F-MD after the first two mechanisms. With these experimental and computational results as a background, the discharge dynamics during positive and negative voltage are summarized in Fig. 16. Discharges with both negative and positive polarities begin with a positive streamer directed towards the cathode. This is the precursor to the formation of filamentary microdischarges (F-MDs) across the gap at the apex of the domes, which is the minimum gap between the two dielectrics. While similar combinations of positive streamer and filamentary microdischarges generate plasma in conventional parallel plate DBDs, in the case of the packed DBD, the generation of the streamer and F-MDs are usually at the location of the minimum gap and only happen once during each half cycle. This phase is followed by the SIW travelling over the dielectric surface from the center of the dome (or the location on the flat dielectric facing the dome) towards the side. With a positive polarity, the SIW propagates over the curved dielectric dome and in the negative cycle the SIW propagates over the plane top dielectric. There is a weaker SIW on the opposite dielectric for both polarities, on the flat and curved dielectrics during the positive and negative polarity, respectively. SIWs on adjacent domes may merge before reaching the contact point. For both polarities, the SIW from the sides result in S-MD either at the contact point or at the location on the flat dielectric axially opposite the contact point. The second current pulse starts as SIWs propagate across the dielectric and current peaks when the opposing SIWs merge at the

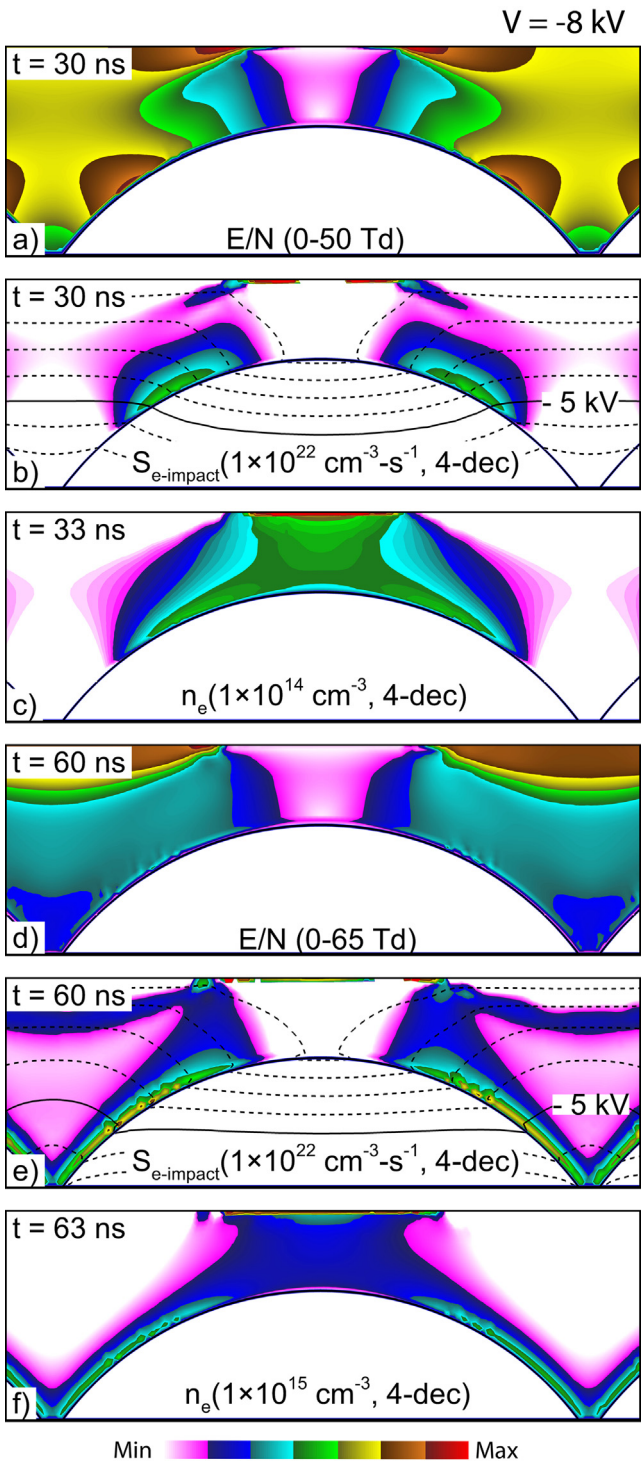

Fig. 14. Reduced electric field, electron impact ionization source term, electron density for −8 kV applied potential. Electric potential lines are overlaid over electron impact ionization source term contour plots, with each line representing a 1 kV change. Times and peak plotted values are noted in the figures.

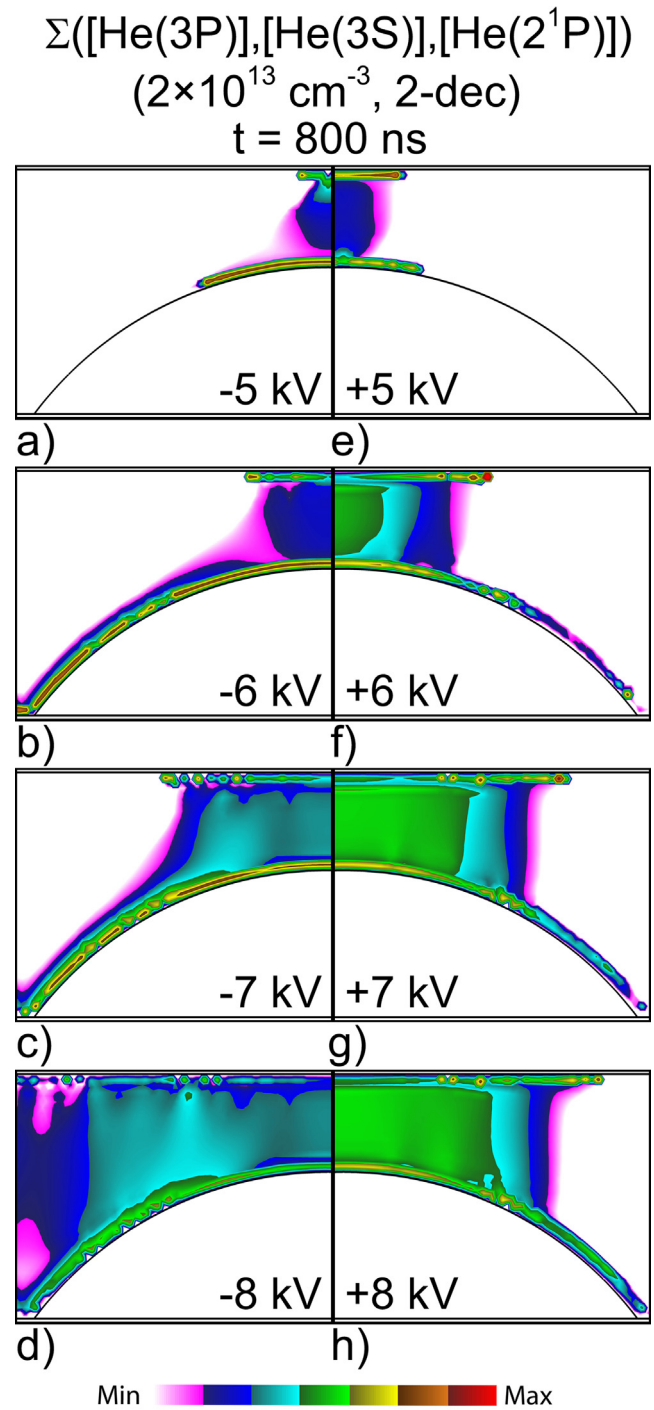

Fig. 15. Sums of the densities of excited species of Helium emitting in the visible spectrum at 800 ns, and at different applied voltages.

contact point. For sufficiently high voltage, multiple current pulses may be generated with the number of current pulses increasing with voltage. Each current pulse results from microdischarges either as S-MDs or a combination of S-MDs and F-MDs. These S-MDs and or F-MDs could be more intense at the edges or in the center depending on conditions.

The sensitivity of plasma structures and discharge types on applied voltage shown here can have important broader implications. For example, formation of SIWs leads to higher electron temperatures, and therefore higher rates of ionization and dissociation of strongly-bonded molecules such as N_2. Controlling the formation of SIWs is therefore an additional pathway to selectivity. The proximity of SIWs to catalysts will enable plasma-produced reactive species with short diffusion lengths and lifetimes to interact with surface sites at a greater rate. Careful packing design was also shown to be of importance. The topology of the packing material can determine the direction, morphology and intensity of plasma discharges. These factors will then impact energy efficiency, selectivity and throughput of commercial

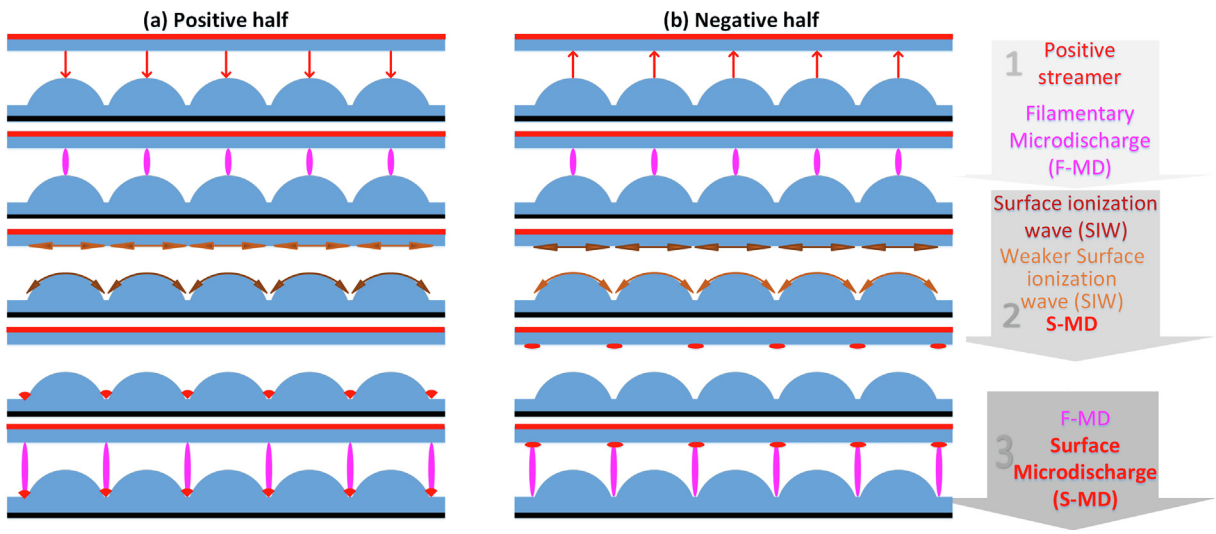

Fig. 16. Schematic representing operation of the discharge for (a) positive and (b) negative polarities of the voltage.

plasma packed bed reactors.

6. Concluding remarks

The dynamics of plasma formation and propagation as a function of applied voltage amplitude and polarity were investigated in a patterned DBD operated in helium through experiments and modeling. The majority of the experimental phenomena were reproduced and explained by the model. The discharge initiates as a positive streamer between the apex of dielectric structure and opposite dielectric plate (at the location of minimum distance), which transforms into a filamentary microdischarge in the gap. The surface charging of the dielectric generates surface-parallel electric fields which enable propagation of surface ionization waves (SIWs) from the apex of the dielectric structure towards the contact points (for the positive polarity). The SIWs across the domes merge at the contact points where the highest electron density is produced, as the smallerdielectric thickness at the contact point produces high capacitance which supports a high surface charge density. The SIW was followed by a restrike or F-MD due to high surface charge resulting in an electric field sufficient for breakdown.

At the lowest voltage, the plasma densities in the F-MDs are relatively low which do not produce a large enough parallel component of the electric field to propagate the SIW, shown in both model and experiment. Experimentally, when increasing the voltage amplitude, the dominant mechanism changed from F-MD to SIW to S-MDs. The model showed that plasma parameters, especially the electron temperature, are very different for each of these mechanisms.

Declaration of Competing Interest

The authors declare that they have no known competing financial interests or personal relationships that could have appeared to influence the work reported in this paper.

Acknowledgements

ZM would like to acknowledge the support of Jazan University Deanship of Scientific Research Project No. 13/6-3299. AH was supported by King Abdulaziz City for Science and Technology (KACST). The work of JK and MJK was supported by the US Department of Energy Office of Fusion Energy Science (DE-SC000319, DE-SC0014132) and the US National Science Foundation (PHY-1519117). ZM would like to thank Julian Schulze for suggestions and useful discussions.

References

[1] K. Schmidtszalowski, A. Borucka, Heterogeneous Effects in the process of ozone synthesis in electrical discharges, Plasma Chem. Plasma Proc. 9 (2) (1989) 235–255.
[2] H.L. Chen, et al., Review of plasma catalysis on hydrocarbon reforming for hydrogen production-Interaction, integration, and prospects, Appl. Catal. B 85 (1–2) (2008) 1–9.
[3] H.L. Chen, et al., Review of packed-bed plasma reactor for ozone generation and air pollution control, Ind. Engr. Chem. Res. 47 (7) (2008) 2122–2130.
[4] M. Kraus, et al., CO2 reforming of methane by the combination of dielectric-barrier discharges and catalysis, PCCP 3 (3) (2001) 294–300.
[5] D. Mei, et al., Plasma-assisted conversion of CO_2 in a dielectric barrier discharge reactor: understanding the effect of packing materials, Plasma Source Sci. Technol. (2015) 24(1).
[6] A. Gomez-Ramirez, et al., Improving the pollutant removal efficiency of packed-bed plasma reactors incorporating ferroelectric components, Chem. Engr. J. 314 (2017) 311–319.
[7] J.C. Whitehead, Plasma-catalysis the known knowns, the known unknowns and the unknown unknowns, J. Phys. D Appl. Phys. 49 (24) (2016).
[8] H.-H. Kim, et al., Plasma catalysis for environmental treatment and energy applications, Plasma Chem. Plasma Proc. 36 (1) (2016) 45–72.
[9] K. Van Laer, A. Bogaerts, Fluid modelling of a packed bed dielectric barrier discharge plasma reactor, Plasma Source Sci. Technol. 25 (1) (2016) 015002.
[10] K. Van Laer, A. Bogaerts, How bead size and dielectric constant affect the plasma behaviour in a packed bed plasma reactor: a modelling study, Plasma Source Sci. Technol. 26 (8) (2017) 085007.
[11] J. Kruszelnicki, et al., Propagation of negative electrical discharges through 2-dimensional packed bed reactors, J. Phys. D Appl. Phys. 50 (2) (2017) 025203.
[12] H.J. Gallon, et al., Microscope–ICCD imaging of an atmospheric pressure CH4 and CO2 dielectric barrier discharge, Trans. Plasma Sci. 39 (11) (2011) 2176–2177.
[13] H.H. Kim, A. Ogata, Nonthermal plasma activates catalyst: from current understanding and future prospects, Euro. Phys. J.-Appl. Phys. 55 (1) (2011) 13806.
[14] H.-H. Kim, J.-H. Kim, A. Ogata, Microscopic observation of discharge plasma on the surface of zeolites supported metal nanoparticles, J. Phys. D Appl. Phys. 42 (13) (2009) 135210.
[15] H.-H. Kim, Y. Teramoto, A. Ogata, Time-resolved imaging of positive pulsed corona-induced surface streamers on TiO2 and γ-Al_2O_3-supported Ag catalysts, J. Phys. D Appl. Phys. 49 (41) (2016) 415204.
[16] H.-H. Kim, et al., Effects of Si/Al ratio on the interaction of nonthermal plasma and Ag/HY catalysts, Appl. Catal B 166 (2015) 9–17.
[17] W. Wang, et al., Streamer propagation in a packed bed plasma reactor for plasma catalysis applications, Chem. Engr. J. 334 (2018) 2467–2479.
[18] W.S. Kang, et al., Surface streamer propagations on an alumina bead: experimental observation and numerical modeling, Plasma Source Sci. Technol. 27 (1) (2018) 015018.
[19] T. Butterworth, R.W.K. Allen, Plasma-catalyst interaction studied in a single pellet DBD reactor: dielectric constant effect on plasma dynamics, Plasma Source Sci. Technol. 26 (6) (2017) 065008.
[20] Z. Mujahid, A. Hala, Plasma dynamics in a packed bed dielectric barrier discharge (DBD) operated in Helium, J. Phys. D Appl. Phys. 51 (2018) p. 11LT02.
[21] D. Mei, X. Tu, Conversion of CO_2 in a cylindrical dielectric barrier discharge reactor: Effects of plasma processing parameters and reactor design, J. CO_2 Util 19 (2017) 68–78.
[22] R. Aerts, W. Somers, A. Bogaerts, Carbon Dioxide Splitting in a Dielectric Barrier Discharge Plasma: A Combined Experimental and Computational Study, ChemSusChem 8 (4) (2015) 702–716.

[23] L. Bischoff, et al., Experimental and computational investigations of electron dynamics in micro atmospheric pressure radio-frequency plasma jets operated in He/N_2 mixtures, Plasma Source Sci. Technol. 27 (12) (2018) 125009.
[24] M. Zaka-ul-Islam, Dynamics of a pulsed inductively coupled oxygen plasma, Phys. Plasma 23 (11) (2016) 113505.
[25] M. Zaka-ul-Islam, et al., Electron dynamics and frequency coupling in a radio-frequency capacitively biased planar coil inductively coupled plasma system, Plasma Source Sci. Technol. 24 (4) (2015) 044007.
[26] M. Zaka-ul-Islam, et al., Energetic electron avalanches and mode transitions in planar inductively coupled radio-frequency driven plasmas operated in oxygen, Appl. Phys. Lett. 99 (4) (2011) 041501.
[27] S.A. Norberg, et al., Formation of reactive oxygen and nitrogen species by repetitive negatively pulsed helium atmospheric pressure plasma jets propagating into humid air, Plasma Sources Sci. Technol. 24 (3) (2015) 035026.
[28] Y.P. Raizer, J.E. Allen, Gas Discharge Physics, Springer, Berlin, 1997.
[29] F. Massines, et al., Glow and Townsend dielectric barrier discharge in various atmosphere, Plasma Phys. Cont. Fusion 47 (12B) (2005) B577.
[30] H. Höft, et al., Breakdown characteristics in pulsed-driven dielectric barrier discharges: influence of the pre-breakdown phase due to volume memory effects, J. Phys. D Appl. Phys. 47 (46) (2014) 465206.
[31] T. Briels, et al., Positive and negative streamers in ambient air: measuring diameter, velocity and dissipated energy, J. Phys. D Appl. Phys. 41 (23) (2008) 234004.